International Journal of Mass Spectrometry 354–355 (2013) 87–98

Contents lists available at ScienceDirect

International Journal of Mass Spectrometry

journal homepage: www.elsevier.com/locate/ijms

Guided ion-beam and theoretical studies of the reaction of Os^+ (^6D) with O_2: Adiabatic and nonadiabatic behavior

Christopher S. Hinton[1], Murat Citir[2], P.B. Armentrout*

Chemistry Department, University of Utah, 315 S. 1400 E. Rm 2020, Salt Lake City, UT 84112, United States

ARTICLE INFO

Article history:
Received 26 March 2013
Received in revised form 11 May 2013
Accepted 15 May 2013
Available online 30 May 2013

Dedicated to Detlef Schröder, a great scientist, colleague, and friend.

Keywords:
Bond energy
Osmium oxide
Spin conservation
Thermochemistry

ABSTRACT

The kinetic-energy dependence of the $Os^+ + O_2$ reaction is examined using guided ion-beam mass spectrometry. The cross section for OsO^+ formation from ground state Os^+ (^6D) is unusual, exhibiting two endothermic features. The kinetic energy dependence for OsO^+ formation is analyzed to determine $D_0(Os^+—O) = 4.96 \pm 0.02$ eV, with the higher energy feature having a threshold 1.36 ± 0.11 eV higher in energy. This bond energy is roughly consistent with previous values determined by bracketing measurements. Formation of OsO_2^+ is also observed with a pressure dependent cross section, establishing that it is formed in an exothermic reaction of OsO^+ with O_2. The nature of the bonding for OsO^+ and OsO_2^+ is discussed and analyzed primarily using theoretical calculations at the B3LYP/def2-TZVPPD level of theory. The ground state of OsO^+ is identified as either $^6\Sigma^+$ or $^4\Pi$, with the latter favored once estimates of spin-orbit splitting are included. Bond energies for ground state OsO^+ are calculated at this level as well as BHLYP, BLYP, BP86, and CCSD(*T*,full) levels along with using the Stuttgart–Dresden (SDD) and Hay–Wadt (HW+) basis sets on osmium with a 6-311+G(3df) basis on oxygen. BLYP and BP86 theoretical bond energies are higher than the experimental value, whereas B3LYP and CCSD(*T*,full) values are lower, and BHLYP values are much too low. Potential energy surfaces for the reaction of Os^+ with O_2 are also calculated at the B3LYP/def2-TZVPPD level of theory and reveal that ground state Os^+ (^6D) inserts into O_2 by forming a $Os^+(O_2)$ ($^4B_2$) complex which can then couple with additional surfaces to form ground state OsO_2^+ ($^2B_1$). Several explanations for the unusual dual endothermic features are explored, with no unambiguous explanation being evident. As such, this heavy metal system provides a very interesting experimental phenomenon of both adiabatic and nonadiabatic behavior.

1. Introduction

The properties of transition metal oxides have been widely studied [1–4] because of their use as catalysts in oxidation processes. An important example is OsO_4, which can be used in organic synthesis to add two hydroxyl groups across an alkene double bond with cis stereochemistry [5]. The examination of such oxidation processes as a means to convert methane to more readably accessible chemicals has garnered significant interest [6–10], with Schröder and Schwarz providing comprehensive reviews of such processes in the gas phase [11,12]. The gas phase is an ideal arena for detailed study of the energetics of bond-making and bond-breaking processes at a molecular level. Because solvent, metal supports, and their interactions are absent, quantitative thermodynamic and intrinsic mechanistic information for various bond activation processes can be obtained. For osmium in particular, Irikura and Beauchamp have demonstrated that Os^+, OsO^+, OsO_2^+, and OsO_4^+ all activate methane, albeit by different pathways: dehydrogenation by Os^+ and OsO^+, dehydration by OsO_2^+, and H atom abstraction by OsO_4^+ [13]. Recent theoretical work has explored the pathways for the reactions of OsO_n^+ ($n = 1$–4) with methane computationally [14].

Surprisingly, the thermochemistry of OsO^+ is poorly known, even though there are several experimental and theoretical studies in the literature on OsO^+. Early experiments by Dillard and Kiser performed electron impact studies on osmium tetroxide and from the difference in appearance energies for Os^+, OsO^+, and OsO_2^+ determined an $Os^+—O$ bond dissociation energy (BDE) of 5.6 ± 0.5 eV and an $OOs^+—O$ BDE of 4.1 ± 0.3 eV [15]. Similar experiments by Watson et al. lead to values of 4.9 ± 1.2 eV and 5.4 ± 0.7 eV, respectively [16]. Irikura and Beauchamp performed Fourier transform ion cyclotron resonance (FT-ICR) studies on reactions of the fragment ions of OsO_4 with a multitude of species. On the basis of exothermic oxygen atom transfer reactions observed between OsO^+ and C_2H_4 and OsO_2^+ and H_2, they determined upper limits of 4.86 eV and 5.09 eV for the BDEs of OsO^+ and OsO_2^+, respectively.

* Corresponding author. Tel.: +1 801 581 7885.
E-mail address: armentrout@chem.utah.edu (P.B. Armentrout).
[1] Present address: Institute for Scientific Research, Boston College, Chestnut Hill, MA 02467, United States.
[2] Present address: Abdullah Gül University, Melikgazi/Kayseri 38039, Turkey.

1387-3806/$ – see front matter © 2013 Elsevier B.V. All rights reserved.
http://dx.doi.org/10.1016/j.ijms.2013.05.015

Consideration of the sequential bond energies for OsO_4^+ then permitted reasonable lower limits to be ascertained, such that they assigned BDEs of 4.34 ± 0.52 eV and 4.57 ± 0.52 eV, respectively [13]. Inductively coupled plasma/selected ion flow tube (ICP/SIFT) experiments by Bohme and coworkers found that ground state Os^+ reacted slowly with O_2 to form OsO_2^+ and that reaction (1)

$$Os^+ + O_2 \rightarrow OsO^+ + O \quad (1)$$

occurred only for excited states of Os^+ at thermal energies [17]. Similarly, Schweikhard and coworkers have examined the thermal reactions of Os^+ with O_2 in a Penning ion trap [18] and FT-ICR [19]. They too determined that only excited Os^+ ions react with O_2 to form OsO^+ and that the OsO^+ product reacted subsequently to form OsO_2^+ in reaction (2).

$$OsO^+ + O_2 \rightarrow OsO_2^+ + O \quad (2)$$

Additionally, there are several theoretical papers on OsO^+ in the literature [14,20–22].

The present study is designed to provide more quantitative information about OsO^+. By using guided ion beam tandem mass spectrometry (GIBMS), the energetics, kinetics, and dynamics of the interaction of osmium metal with O_2 can be obtained. In previous studies in our laboratory, GIBMS has been used to systematically study the kinetic energy dependent reactions of O_2 with atomic cations of the first-row [23–31], second-row [25,29,32–37], and third-row [29,38–42] transition metals and main group metals [43–45]. In many cases, analyses of the cross sections for the analogs of reaction (1) have enabled determination of the BDEs of the metal oxide cation, MO^+. The present work extends these studies to include the metal ion Os^+, and as such, is part of an ongoing effort in our laboratory to understand the periodic trends in the BDEs of metal oxides. As will be seen below, the kinetic energy dependent cross section for reaction (1) is unusual, exhibiting two strong endothermic features. The reasons behind this behavior are explored in terms of spin-conservation and adiabatic versus nonadiabatic behavior.

2. Experimental and theoretical section

2.1. General experimental

The guided ion beam tandem mass spectrometer on which these experiments were performed has been described in detail previously [46,47]. Briefly, atomic osmium ions are generated in a direct current discharge flow tube (DC/FT) source described below, extracted from the source, accelerated, and focused into a magnetic sector momentum analyzer for mass selection of primary ions. The mass-selected ions are decelerated to a desired kinetic energy and focused into an octopole ion beam guide that uses radio-frequency (rf) electric fields to trap the ions in the radial direction and ensure complete collection of reactant and product ions [48,49]. The octopole passes through a static gas cell with an effective length of 8.26 cm that contains the reaction partner (here, O_2) at a low pressure (usually less than ~0.4 mTorr) so that multiple ion–molecule collisions are improbable. The unreacted parent and product ions are confined radially in the guide until they drift to the end of the octopole where they are extracted, focused, and passed through a quadrupole mass filter for mass analysis of products. Ions are subsequently detected with a secondary electron scintillation ion detector [50] using standard pulse counting techniques. Reaction cross sections are calculated from product ion intensities relative to reactant ion intensities after correcting for background signals [51]. Uncertainties in absolute cross sections are estimated to be ±20%.

The kinetic energy of the ions is varied in the laboratory frame by scanning the dc bias on the octopole rods with respect to the potential of the ion source region. Laboratory (lab) ion energies are converted to energies in the center-of-mass frame (CM) by using the formula $E_{CM} = E_{lab} \times m/(m+M)$, where m and M are the neutral and ionic reactant masses, respectively. Two effects broaden the cross section data: the kinetic energy distribution of the reactant ion and the thermal motion of the neutral reactant gas (Doppler broadening) [52]. The absolute zero and the full width at half maximum (FWHM) of the kinetic energy distribution of the reactant ions are determined using the octopole beam guide as a retarding potential analyzer, as described previously [51]. The distributions of ion energies, which are independent of energy, are nearly Gaussian and have a typical FWHM of 0.4–0.5 eV (lab) in these studies. Uncertainties in the absolute zero of the energy scale are ± 0.1 eV (lab) and ± 0.014 eV (CM).

2.2. Ion source

Os^+ ions are produced in a DC/FT source [47], consisting of a cathode held at a high negative voltage (1.2–1.6 kV) over which a flow of approximately 90% He and 10% Ar passes at a total pressure of 0.3–0.5 Torr. The dc-discharge ionizes Ar and then accelerates these ions into the cathode made of iron with a osmium/vanadium alloy disk attached to the cathode. All experiments were conducted with the most abundant isotope, ^{192}Os at 40.8%. As the ions are swept down the meter-long flow tube, they undergo ~10^5 thermalizing collisions with He and Ar. The presence of excited electronic states can often be observed as low-energy features in the cross sections. No such features were observed in previous studies of Os^+ with H_2, HD, and D_2 [53] nor in ongoing work with CH_4 and CD_4. In addition, results were checked by adding N_2O to the flow tube as a cooling gas with no change in the cross sections observed. When compared to a surface ionization source, the DC/FT source has been found to generate Sc^+ [54], Fe^+ [55], Co^+ [56], Ni^+ [57], Ru^+ [58], Rh^+ [58], and Pd^+ [58] ions with an average electronic temperature of 700 ± 400 K, and Y^+, Zr^+, Nb^+, and Mo^+ ions with an average electronic temperature of 300 ± 100 K [59]. Therefore, Os^+ ions created under such conditions are believed to be in the ground state electronic term, ^6D ($6s^15d^6$) [60,61], and largely in the lowest spin-orbit level (Table 1). These estimated populations are consistent with the failure to observe any evidence for electronically excited Os^+ species in previous studies [53] and lead to a negligible uncertainty (<0.01 eV) in the electronic energy of the Os^+ reactant.

2.3. Data analysis

The cross sections of endothermic reactions are modeled using Eq. (3) [62–65],

$$\sigma(E) = \sigma_0 \sum \frac{g_i(E + E_i - E_0)^n}{E^m} \quad (3)$$

where σ_0 is an energy-independent scaling factor, E is the relative kinetic energy of the reactants, n and m are adjustable parameters that characterize the energy dependence of the process (with m generally set equal to unity) [62], and E_0 is the 0 K threshold for reaction of electronic, vibrational, and rotational ground state reactants. The model involves an explicit sum of the contributions of individual ro-vibrational states of the O_2 reactant ($\nu = 1580\ cm^{-1}$, $B = 1.4456\ cm^{-1}$) [66], denoted by i, having energies E_i and populations g_i. As noted above, contributions from excited electronic states of Os^+ are negligible. Before comparison with the experimental data, Eq. (3) is convoluted with the kinetic energy distributions of the reactant ions and neutrals at 300 K [51]. The σ_0, n, and E_0 parameters are then optimized using a nonlinear least-squares analysis to give the best reproduction of the data. Error limits for E_0 are calculated from the range of threshold values for different

Table 1
Electronic states of atomic osmium cations.

State	Configuration	J	Energy[a] (eV)	Population (%)		
				300 K	700 K	1100 K
^{6}D	$6s^15d^6$	9/2	0.000	100.0	99.931	98.901
		7/2	0.445	0.0	0.050	0.720
		5/2	0.487	0.0	0.019	0.348
		3/2	0.693	0.0	0.000	0.026
		1/2	0.823	0.0	0.000	0.003
^{6}S	$6s^25d^5$	5/2	0.978	0.0	0.000	0.002
^{4}D	$6s^15d^6$	avg	1.475[b,c]	0.0	0.000	0.000
^{4}F	$5d^7$	avg	1.648[b,d]	0.0	0.000	0.000

[a] From Ref. [60], except as noted.
[b] State assignments from Ref. [61].
[c] Weighted average of spin-orbit levels, 7/2, 5/2, and 3/2 (1/2 missing).
[d] Weighted average of spin-orbit levels, 7/2 and 5/2 (9/2 and 3/2 missing). Also the 7/2 level (at 1.637 eV) should lie at the energy of the ^{4}F state before spin-orbit splitting in the absence of perturbations from other states.

data sets over a range of acceptable n values combined with the absolute uncertainty in the kinetic energy scale.

2.4. Theoretical calculations

Most quantum chemistry calculations reported here were computed using the B3LYP hybrid density functional method and performed with the GAUSSSIAN 09 suite of programs [67]. The B3LYP method is based on the hybrid gradient-corrected exchange functional proposed by Becke [68] combined with the gradient-corrected correlation functional of Lee et al. [69]. Additional density functionals used include Becke half-and-half LYP [70] (BHLYP), BLYP [71], and BP86 [72], along with coupled cluster with single, double, and perturbative triple excitation (CCSD(T,full)) [73–76]. Here, the BP86 functional is chosen specifically because it was found to perform well for a variety of transition metal complexes [77] and has been found to yield reasonable upper limits on the thermochemistry of organometallic species in previous work, where B3LYP gives reasonable lower limits [78]. The def2-TZVPPD basis set was used for oxygen in most calculations, with very similar results obtained in earlier calculations using the 6-311+G(3df) basis set [79] both being triple-ζ with diffuse and polarization functions. These basis sets give good results for the thermochemistry of O_2 with an O—O bond energy calculated using B3LYP as 5.26 and 5.28 eV, respectively, compared to the experimental value of 5.115 eV, Table 2 [80]. Notably other approaches fare less well with BHLYP yielding very low values (near 4.3 eV), and BLYP and BP86 yielding high values (near 5.8 and 6.1 eV, respectively). Even the CCSD(T,full) approach is off somewhat with bond energies of 4.88 eV and 4.96 eV for the two basis sets, respectively. Increasing the size of the basis set to def2-QZVPPD leads to excellent agreement for CCSD(T,full) with a bond energy of 5.04 eV, while this basis set affects the results for the four DFT approaches very little, Table 2.

For osmium, several basis sets were used, all using relativistic effective core potentials (ECPs) that are small core (60 electrons) such that the 5s, 5p, 5d, and 6s orbitals are explicitly considered. The def2-QZVPPD, def2-TZVPPD (which is equivalent to def2-TZVPP) [81], and Stuttgart–Dresden (SDD) [82] use ECPs developed by Andrea et al. [83], whereas the HW+ basis set uses that of Hay–Wadt (HW) [84]. The def2 basis sets include f and g type polarization functions on Os, whereas neither the HW+ nor SDD basis set do. (The def2 and SDD basis sets were obtained from the basis set exchange of the Environmental and Molecular Sciences Laboratory, EMSL [85,86].) The HW-ECP is optimized for neutral atoms, whereas the HW+ basis used here was developed by Ohanessian et al. [87] to account for the differential contraction of the s orbitals compared to the d orbitals resulting from the positive charge. In all cases, the thermochemistry calculated and cited here for OsO^+ and OsO_2^+ is corrected for zero point energy effects, after scaling the frequencies by 0.989 [88].

One means of testing the validity of the theoretical results is to compare the theoretical results for the excitation energies of the various states of Os^+ to experimentally measured values, Table 2. Experimentally, the weighted average over all spin-orbit levels for the ^{6}D ($6s^15d^6$) ground state is 0.363 eV above the $^6D_{9/2}$ ground level, Table 1. Experimental excitation energies (again weighted averages over all spin-orbit levels) to the ^{6}S ($6s^25d^5$), ^{4}D ($6s^15d^6$), and ^{4}F ($5d^7$) excited states are 0.615, 1.112, and 1.285 eV, respectively (Table 1). Note that the values for the quartet states are somewhat tenuous because some spin-orbit levels have not been identified. Calculations properly identified the ground state as the ^{6}D except for CCSD(T,full) calculations using the SDD and HW+ basis sets, Table 2. In contrast, the CCSD(T,full) calculations using the def2 basis sets yield excitation energies in reasonable agreement with experiment, with average deviations below 0.2 eV. Thus, the lack of f- and g-polarization functions suggest that the HW+ and SDD basis sets are insufficient for a meaningful recovery of electron correlation at the CCSD(T,full) level. The DFT/HW+ calculations also perform reasonably well with average deviations below 0.2 eV, with BHLYP/HW+ having an average deviation below 0.1 eV. Overall, the CCSD(T,full)/def2 calculations appear to yield the best performance.

3. Results

3.1. Reaction of Os^+ with O_2

Fig. 1 shows cross sections for the reaction of Os^+ with O_2 at a pressure of 0.42 mTorr yielding OsO^+ and OsO_2^+ as a function of kinetic energy. The OsO^+ cross section exhibits two features. The first feature has an apparent threshold near 0 eV, reaches a maximum near 0.4 eV and then starts to decline. The second feature has an apparent threshold near 1.2 eV, reaches a maximum near 5 eV, and then starts to decline because the OsO^+ product ion can dissociate further in reaction (4),

$$Os^+ + O_2 \rightarrow OsO^+ + O \rightarrow Os^+ + O + O \quad (4)$$

which has a thermodynamic threshold of 5.115 eV = $D_0(O_2)$. Notably the endothermicity of reaction (1) observed here agrees with the observations of Bohme and coworkers and Schweikhard and coworkers, in which an excited state of Os^+ was needed in order to form OsO^+ at thermal energies [17–19]. Our cross sections for reaction (1) at thermal energy can be converted to a rate coefficient of $5 \pm 1 \times 10^{-12}$ cm^3 molecule^{-1} s^{-1}, two orders of magnitude smaller than the collision limit, which is small enough to agree with the failure to observe this process in the previous studies.

Table 2
Bond energy of O_2 ($^3\Sigma^-$) and excitation energies for the atomic osmium ion (eV) calculated at several levels of theory.

State	Basis set	B3LYP	BHLYP	BLYP	BP86	CCSD(T,full)	Exp.
$D_0(O_2, {}^3\Sigma_g^-)$	def2-QZVPPD	5.27	4.27	5.80	6.07	5.04	5.12
	def2-TZVPPD	5.26	4.25	5.79	6.06	4.88	
	G	5.28	4.28	5.81	6.08	4.96	
$^6D(6s^15d^6)$	def2-QZVPPD	0.0	0.0	0.0	0.0	0.0	0.00[a]
	def2-TZVPPD	0.0	0.0	0.0	0.0	0.0	
	SDD	0.0	0.0	0.0	0.0	2.54	
	HW+	0.0	0.0	0.0	0.0	0.49	
$^6S(6s^25d^5)$	def2-QZVPP	1.00	0.96	0.97	–	0.73	0.62[a]
	def2-TZVPP	1.01	0.97	0.98	1.25	0.79	
	SDD	1.05	1.01	1.03	1.25	2.82	
	HW+	0.70	0.60	0.72	0.95	0.60	
$^4D(6s^15d^6)$	def2-QZVPP	1.18	1.14	0.82	0.98	0.97	1.11[a]
	def2-TZVPP	1.18	1.14	1.14	1.50	0.92	
	SDD	0.81	0.83	0.77	0.94	0.0	
	HW+	1.05	1.13	0.97	1.11	0.0	
$^4F(5d^7)$	def2-QZVPP	0.75	0.82	0.68	0.77	0.90	1.28[a]
	def2-TZVPP	0.76	0.82	0.81	0.80	0.88	
	SDD	0.76	0.82	0.69	0.79	1.98	
	HW+	0.92	1.03	0.82	0.89	1.84	

[a] Statistically weighted mean of spin-orbit levels. Referenced to the ground term, 0.363 eV above the $^6D_{9/2}$ level. See Table 1 for references.

Fig. 1 also shows the cross section for the formation of OsO_2^+. The magnitude of this cross section was found to depend linearly on O_2 pressure, such that it disappears when extrapolated to zero pressure. Thus, this product is formed in the sequential reaction (2) or by a termolecular association process. We exclude the latter process because Koyanagi et al. find the termolecular process in He at 0.35 Torr has an apparent bimolecular rate constant of only 3.7×10^{-12} cm^3 s^{-1} [17], such that the termolecular process with an O_2 pressure that is three orders of magnitude smaller would not be observed. More insight into this process can therefore be obtained by interpreting the raw data as if the OsO^+ species is the reactant and the intensities are again converted to an absolute cross section. Fig. 2 shows the data taken at $P(O_2) = 0.42$ mTorr interpreted in this fashion. Data taken at $P(O_2) = 0.19$ mTorr is quantitatively similar in magnitude and energy dependence but more scattered. It should be realized that this interpretation is not precisely correct in that the kinetic energy of the OsO^+ product is no longer accurately reflected by the energy axis shown (that of the $Os^+ + O_2$ reactants). Nevertheless, the OsO_2^+ cross section obtained falls off uniformly with energy below 1.5 eV, with an energy dependence below 0.5 eV comparable to that expected for ion-neutral collisions according to the Langevin–Gioumousis–Stevenson (LGS) model [89], Eq. (5),

$$\sigma_{LGS} = \pi e \left(\frac{\alpha}{2\pi\varepsilon_0 E} \right)^{1/2} \quad (5)$$

where e is the charge on the electron, α is the polarizability volume of the neutral reactant molecule (1.57 Å^3 for O_2) [90], and ε_0 is the permittivity of vacuum. The experimentally observed magnitude for the cross section of reaction (2) is about 16 ± 3% of the collision prediction. Our results are consistent with those of Schweikhard and coworkers that OsO^+ reacts with O_2 at thermal energies, although they obtain a rate constant of $5.0 \pm 0.3 \times 10^{-11}$ cm^3 molecule^{-1} s^{-1} [19]. (Here the quoted uncertainty is only the statistical uncertainty, whereas a systematic uncertainty is probably on the order of 1.0×10^{-11} cm^3 molecule^{-1} s^{-1}.) Compared to the collision rate, $k_{LGS} = 5.6 \times 10^{-10}$ cm^3 molecule^{-1} s^{-1}, this indicates a reaction efficiency of 9 ± 2%, which is somewhat lower than our value. Some deviations in these measurements can be expected because of the uncertainty in our energy scale and, in the FT-ICR experiments, the OsO^+ is formed by thermal reactions of electronically excited Os^+,

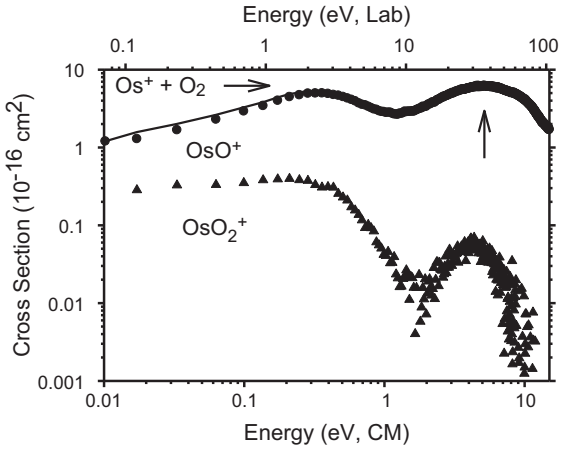

Fig. 1. Cross sections for the reaction of Os^+ (^6D) with O_2 at a pressure of 0.42 mTorr as a function of kinetic energy in the center-of-mass frame (lower axis) and laboratory frame (upper axis). Formation of OsO^+ (circles), OsO_2^+ (triangles), and their total (line) are indicated. The arrow shows the O_2 bond energy at 5.115 eV.

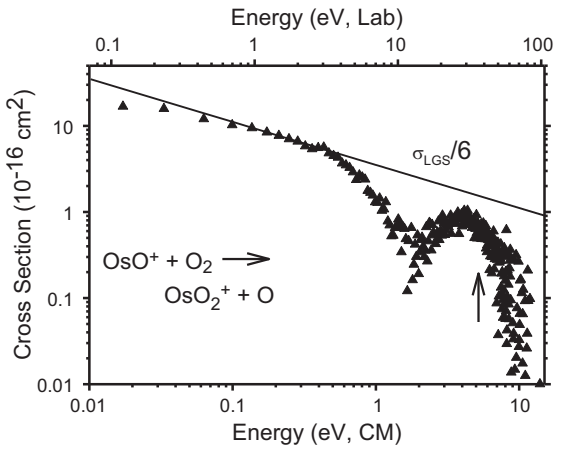

Fig. 2. Estimated cross section for reaction (2) determined as described in the text as a function of kinetic energy in the center-of-mass (lower axis) and laboratory (upper axis) frames. The arrow indicates the O_2 bond energy at 5.115 eV. The line shows the Langevin–Gioumousis–Stevenson collision cross section divided by six.

which can alter the internal energy of the OsO^+ reactant compared with that formed in our work.

The cross section for reaction (2) shown in Fig. 2 also exhibits a high energy feature starting about 1.8 eV. Although it is possible that this corresponds to formation of an excited state of OsO_2^+, it is also plausible that this simply follows from the second feature in the primary OsO^+ product cross section. This latter possibility recognizes the fact that the OsO^+ products formed at threshold in this second feature have little kinetic energy and hence should react efficiently in an exothermic process. This is again a reflection that the energy scale shown may not be accurate.

3.2. Analysis of the OsO^+ cross section

The first endothermic feature in the OsO^+ cross section presumably corresponds to the formation of ground state OsO^+ in reaction (1). This process has an apparent threshold near 0 eV, peaks around 0.4 eV, and falls to approximately 50% of its maximum intensity before the rise of a second endothermic feature near 1.2 eV. Notably, this decline in the cross section at low energies cannot be attributed to decomposition of the product ion, as reaction (4) is inaccessible below $D_0(O_2) = 5.115$ eV. Furthermore, because no products other than $OsO^+ + O$ are feasible in this energy range, the second feature is plausibly assigned to the formation of electronically excited products. The energy difference between the two features is smaller than the excitation of the O neutral product, which requires 1.97 eV to form the ^1D state [91]. Therefore, we tentatively assign the second cross section feature to the formation of electronically excited OsO^+, an assumption explored thoroughly below.

The kinetic-energy dependence observed in the low energy part of the OsO^+ cross section is unusual. Although it is energetically possible to form excited states in most ion–molecule reactions at elevated kinetic energies, it is unusual for individual product states to give rise to distinct features in GIB experiments. Clearly, the routes to the two products in question must differ in some fundamental way. In previous work, we have observed a similar phenomenon for reaction of V^+ with CS_2 [92]. Again two features were observed in the cross section for formation of VS^+, with the lower energy feature peaking sharply at low energies. Here, the two features were attributed to reactions (6) and (7).

$$V^+(^5D) + CS_2(^1\Sigma_g^+) \rightarrow VS^+(^3\Sigma^-) + CS(^1\Sigma^+) \quad (6)$$

$$V^+(^5D) + CS_2(^1\Sigma_g^+) \rightarrow VS^+(^5\Pi) + CS(^1\Sigma^+) \quad (7)$$

Here, formation of the VS^+ ($^3\Sigma^-$) ground state is spin forbidden, whereas formation of VS^+ ($^5\Pi$) is spin-allowed, which can explain why the latter process is easily observed as a distinct feature in the cross section even though it is much more endothermic than the former process. This work also demonstrated that the sharp peak in the cross section for reaction (6) could be explained by the energy dependence of the spin-orbit coupling needed to permit this reaction to occur. Within a Landau–Zener framework, this leads specifically to $\sigma_{LZ}(E) = \sigma(E)/E^{1/2}$, which can be represented using Eq. (3) by letting m be 0.5 greater than its usual value of $m = 1.0$. A related phenomena was observed in the reaction of S^+ (^4S) + $H_2 \rightarrow SH^+(^3\Sigma^-)$ + H (^2S) [93], where two endothermic features were again observed with the low energy one peaking sharply. Here, the higher energy feature could be explained as a spin-allowed reaction along a quartet surface exhibiting a barrier, whereas the lower energy feature requires changing to the doublet surface associated with the ground state of the H_2S^+ ($^2B_1$) intermediate. On the basis of these comparisons, the behavior observed for the formation of OsO^+ in reaction (1) is consistent with a spin-forbidden reaction at low energies followed by a spin-allowed reaction at higher energies.

Table 3
Parameters of Eq. (3) used to model reaction (1).[a]

σ_0	m	n	E_0 (eV)
3.3 ± 0.2	1.0	$0.3_5 \pm 0.05$	$0.16_1 \pm 0.04_0$
3.2 ± 0.2	1.5	$0.6_9 \pm 0.1$	$0.15_6 \pm 0.02_6$
3.2 ± 0.2	2.0	$1.0_4 \pm 0.1$	$0.15_4 \pm 0.02_2$
7.3 ± 0.6	1.0	$1.0_5 \pm 0.06$	1.52 ± 0.11

[a] Uncertainties are two standard deviations.

The endothermic cross sections for reaction (1) are analyzed in detail using Eq. (3) as described above, with optimum values of the fitting parameters listed in Table 3. In the low energy region, multiple data sets and zero pressure extrapolated data were analyzed using Eq. (3) and m values of 1.0, 1.5, and 2.0. As noted above, a value of $m = 1$ is generally sufficient to reproduce the energy dependence of reaction cross sections [62], whereas $m = 1.5$ includes the approximate Landau–Zener energy dependence [92], and $m = 2$ was tried to provide a feel for what range of m values might be useful. To reproduce the data over the range of 0–1 eV, the values of the parameter n then vary as 0.35 ± 0.05, $0.6_9 \pm 0.1$, and $1.0_4 \pm 0.1$, respectively. The quality of the reproduction was comparable for $m = 1.5$ and 2.0, and slightly worse for $m = 1.0$. Fig. 3 shows zero-pressure extrapolated data reproduced using the model with $m = 1.5$. Notably the E_0 threshold values vary little with the n and m parameters, Table 3, yielding an average value of $0.15_7 \pm 0.02_4$ eV (two standard deviations).

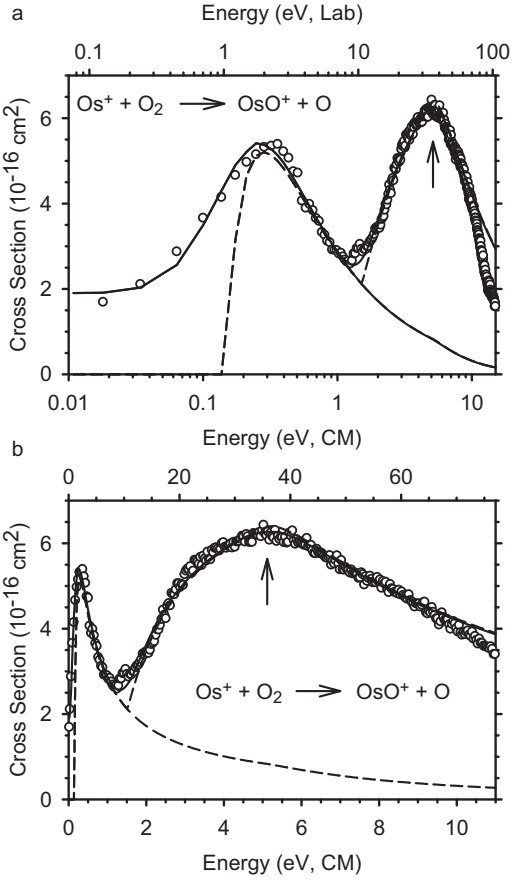

Fig. 3. Zero-pressure extrapolated cross sections for reaction (1) as a function of kinetic energy in the center-of-mass frame (lower axis) and laboratory frame (upper axis) on both log (part a) and linear (part b) scales. The best fits to the data using Eq. (3) with parameters of Table 3 ($m = 1.5$ at low energies) are shown as dashed lines. The solid lines show these models convoluted over the kinetic and internal energy distributions of the reactant neutral and ion. The arrows show the O_2 bond energy at 5.115 eV.

Because the rotational, vibrational, translational, and electronic energy distributions of the reactants are explicitly included in the modeling, the E_0 thresholds determined using Eq. (3) correspond to 0 K. From the thresholds measured, the OsO^+ BDE at 0 K can be calculated using Eq. (8).

$$D_0(Os^+{-}O) = D_0(O{-}O) - E_0 \quad (8)$$

This equation assumes that there are no activation barriers in excess of the endothermicity of reaction (1), an assumption that is often true for ion–molecule reactions because of the long-range attractive forces [51,64]. This assumption is also confirmed by the theoretical calculations of the potential energy surfaces for this reaction (see below). Thus, from the threshold of 0.16 ± 0.02 eV, Eq. (8) indicates that $D_0(OsO^+) = 4.96 \pm 0.02$ eV.

Our bond energy is in rough agreement with the value of 5.6 ± 0.5 eV determined by Dillard and Kiser [15], good agreement with the 4.9 ± 1.2 eV value of Watson et al. [16], but lies slightly above the upper limit of 4.86 ± 0.01 eV determined by Irikura and Beauchamp in FT-ICR studies [13]. This limit was determined on the basis of observing the reaction $OsO^+ + C_2H_4 \rightarrow Os^+ + [C_2,H_4,O]$ at thermal energies; however, the rate of this reaction is not provided, such that it is plausible the reaction is inefficient and occurs as a result of excited (electronically or vibrationally) OsO^+ formed by electron ionization of OsO_4.

If any of the fits to the low energy feature are extended to higher energies and subtracted from the data, the remaining high energy feature can then be analyzed independently. Utilizing all low-energy models ($m = 1$, 1.5, and 2), the high energy feature can be accurately reproduced using Eq. (3) with $m = 1.0$, $n = 1.0_5 \pm 0.06$, and $E_0 = 1.52 \pm 0.11$ eV. The difference in the threshold energies is 1.36 ± 0.11 eV. Modeling of the high energy feature above 5 eV includes consideration of the decline in the cross section associated with reaction (4). A statistical model for this process includes two parameters: the energy onset for reaction (4), E_D, and a parameter p that controls the shape of the cross section in this region [43]. Here, the data are accurately reproduced when E_D is held to $D_0(O_2) = 5.115$ eV, and $p = 0$. Fig. 3 shows that the low-energy feature, the high-energy feature, and the decline in the cross section at high energies are reproduced nicely by these models. Similar reproductions are found for all data sets.

3.3. Theoretical results for OsO^+

B3LYP/def2-TZVPPD calculations performed here indicate that the ground state of OsO^+ is $^6\Sigma^+$ with a bond length of 1.730 Å and a valence electron configuration of $1\sigma^2 1\pi^4 1\delta^2 2\sigma^1 2\pi^2$. In this designation of the molecular orbitals (mos), the Os (5s, 5p) and O (1s, 2s) core electrons are not included, the 1σ and 1π are the Os—O bonding mos, with 2π and 3σ being the antibonding counterparts. The 1δ is pure 5d nonbonding and the 2σ is mostly Os(6s) nonbonding. Given these identifications, the $^6\Sigma^+$ state has six electrons in bonding mos and two in antibonding mos for a bond order of two. This is reasonable given the relatively strong bond energy of 4.96 eV measured here. Further, this bond energy is approximately two-thirds that of HfO^+, TaO^+, and WO^+, 6.91 ± 0.11, 7.10 ± 0.12, and 6.77 ± 0.07 eV, respectively, which have triple metal oxygen bonds [38,39].

In addition to the $^6\Sigma^+$ state, there is also a low-lying $^4\Phi/\Pi$ state that involves moving an electron from the 2π antibonding orbital to the 1δ nonbonding orbital, such that it has a bond order of 2.5 and a shorter bond, 1.657 Å. In previous theoretical studies, the ground state of OsO^+ was usually assigned as the $^6\Sigma^+$. For instance, Yao et al. calculate excitation energies to the quartet state of 0.03 eV and 0.21 eV at the BLYP/SDD/6-311+G(d) and B3LYP/SDD/6-311+G(d) levels, but the quartet is the ground state by unspecified amounts when using B3PW91, BPW91, B3P86, BP86, MPW1PW91, PBE1PBE, and SVWN approaches [20]. Li et al. put the quartet 0.18 eV and 0.10 eV above the sextet at the B3LYP/TZVP and CCSD(*T*,full)/6-311+G(d) levels [21], and Wang et al. calculate an excitation energy of 0.12 eV at the B3LYP/SDD/6-311+G(3df) level [22]. In contrast, Zhang et al. have the quartet being the ground state with the sextet lying only 0.02 eV higher in energy at the B3LYP/LANLDZ+f/6-311G(d) level [14]. Given these low excitation energies, there is obviously some question as to the true identity of the ground state. To test this, we calculated the $^6\Sigma^+$–$^4\Phi/\Pi$ excitation energy at several different levels of theory using several different basis sets (including def2-QZVPPD) with the results compiled in Table 4. For B3LYP, BHLYP, and CCSD(*T*,full) approaches, the $^6\Sigma^+$ remained the ground state with excitation energies to the $^4\Phi/\Pi$ of 0.02–0.43 eV. However, the BLYP and BP86 functionals find the reverse (except for BP86/SDD/G) with the sextet lying above the quartet by 0.01–0.14 eV.

Complicating the ground state assignment is the fact that the $^4\Phi/\Pi$ state should have spin-orbit splitting, which could conceivably drop the lowest spin-orbit level below that of the $^6\Sigma^+{}_{5/2}$ state, which has no first-order spin-orbit interactions. To explore

Table 4
$^6\Sigma^+ \rightarrow {}^4\Pi$ excitation energy and bond energies of OsO^+ ($^6\Sigma^+$) and OsO^+ ($^4\Pi$) (eV) calculated at various levels of theory.

	Basis set[a]	B3LYP	BHLYP	BLYP	BP86	CCSD(*T*,full)
$^6\Sigma^+ \rightarrow {}^4\Pi$ [b]	def2-QZVPPD	0.02 (−0.54)	0.25 (−0.32)	−0.14 (−0.70)	−0.06 (−0.63)	0.09 (−0.47)
	def2-TZVPPD	0.02 (−0.54)	0.25 (−0.32)	−0.14 (−0.71)	−0.07 (−0.64)	0.19 (−0.38)
	def2-TZVPPD/G	0.02 (−0.55)	0.25 (−0.32)	−0.14 (−0.71)	−0.07 (−0.64)	0.10 (−0.46)
	SDD/G	0.13 (−0.44)	0.35 (−0.21)	−0.05 (−0.62)	0.02 (−0.54)	0.43 (−0.14)
	HW+/G	0.10 (−0.47)	0.35 (−0.23)	−0.08 (−0.65)	−0.01 (−0.57)	0.42 (−0.15)
$D_0(OsO^+, {}^6\Sigma^+)$[c]	def2-QZVPPD	**4.48** (4.12)	**3.31** (2.95)	5.18 (4.82)	5.38 (5.02)	**4.44** (4.08)
$D_0(OsO^+, {}^4\Pi)$[b,c]		4.46 (**4.66**)	3.06 (**3.26**)	**5.32 (5.52)**	**5.45 (5.65)**	4.35 (**4.55**)
	def2-TZVPPD	**4.46** (4.10)	**3.29** (2.93)	5.16 (4.80)	5.33 (4.97)	**4.33** (3.97)
		4.44 (**4.64**)	3.04 (**3.24**)	**5.30 (5.50)**	**5.41 (5.61)**	4.15 (**4.35**)
	def2-TZVPPD/G	**4.45** (4.09)	**3.28** (2.92)	5.15 (4.79)	5.34 (4.98)	**4.30** (3.94)
		4.43 (**4.63**)	3.03 (**3.23**)	**5.29 (5.49)**	**5.42 (5.64)**	4.20 (**4.40**)
	SDD/G	**4.27** (3.91)	**3.06** (2.70)	5.00 (4.64)	**5.19** (4.83)	**4.38** (4.02)
		4.14 (**4.34**)	2.71 (**2.91**)	**5.05 (5.25)**	5.16 (**5.36**)	3.95 (**4.15**)
	HW+/G	**4.33** (3.97)	**3.12** (2.76)	5.05 (4.69)	5.26 (4.90)	**4.53** (4.17)
		4.23 (**4.43**)	2.78 (**2.98**)	**5.13 (5.33)**	**5.27 (5.47)**	4.11 (**4.31**)

Bold values indicate the ground state bond energy.

[a] G indicates 6-311 + G(3df) basis set used on oxygen.

[b] Values in parentheses have been corrected for the approximate 0.57 eV spin-orbit splitting of the OsO^+ ($^4\Pi_{5/2}$) state. See text.

[c] Values in parentheses have been decreased by the experimental average energy of all spin-orbit levels for Os^+ (^6D), 0.363 eV. See text.

this possibility further, we note that the spin-orbit splitting of the OsN molecule, isoelectronic with OsO^+, in its $^4\Phi$ state has been measured [94,95]. The $^4\Phi_{7/2}$ and $^4\Phi_{5/2}$ states are split by 979.26 cm^{-1}, which in this case should equal three times the spin-orbit splitting constant, $A(^4\Phi) = 326.42\ cm^{-1}$ (where we assume that $E^{so} = A\ \Lambda\ M_S$ with Λ being the orbital angular momentum quantum number and M_S the spin quantum number associated with a particular $\Omega = \Lambda + M_S$ level [96]). (Note that $A(^4\Phi)$ should be approximately ζ_{5d} (Os)/9–3045 cm^{-1}/9 [95,96] = 338 cm^{-1}, where ζ_{5d} is the atomic spin-orbit constant, in good agreement with the experimental value.) Ignoring any interactions with other states, this places the $^4\Phi_{9/2}$ level $4.5 \times A = 1468.89\ cm^{-1}$ (0.182 eV) below the unperturbed $^4\Phi$ state. If the spin-orbit splitting is similar in OsO^+, then the $^6\Sigma^+_{5/2} \rightarrow {}^4\Phi_{9/2}$ excitation energy should be lowered by this amount. For a $^4\Pi$ state, the spin-orbit splitting constant, $A(^4\Pi)$ should equal ζ_{5d} (Os) and the $^4\Pi_{5/2}$ level should lie $1.5 \times A(^4\Pi) = 4568\ cm^{-1}$ (0.566 eV) below the unperturbed state. In this case, the $^6\Sigma^+_{5/2} \rightarrow {}^4\Pi_{5/2}$ excitation energy should be lowered by this amount. It might also be noted that the internally contracted multireference configuration interaction (CMRCI) calculations of Ram et al. on OsN indicate that the $^4\Pi$ state lies 1800 cm^{-1} = 0.223 eV below the $^4\Phi$ state [94], hence we assume that the low-lying quartet state of OsO^+ is also most accurately designated as $^4\Pi$. The estimated spin-orbit correction for the $^4\Pi_{5/2}$ state means that it becomes the likely ground state for all calculations and basis sets used, Table 4, with the excitation to the $^6\Sigma^+_{5/2}$ state ranging from 0.14 eV to 0.71 eV. The other spin-orbit components of the $^4\Pi$ state, the $\Omega = 3/2$, 1/2, and −1/2 levels, are estimated to have excitation energies of about 0.378, 0.755, and 1.133 eV above the $^4\Pi_{5/2}$ ground level.

The 0 K bond energy of the $^6\Sigma^+$ state calculated at the B3LYP/def2-TZVPPD level of theory is 4.46 eV, somewhat below the 4.96 ± 0.02 eV experimental value determined above. Use of different basis sets (SDD and HW+) and theoretical approaches (BHLYP, BLYP, BP86, and CCSD(*T*,full)) were also explored, with results compiled in Table 4. Clearly, the B3LYP and CCSD(*T*,full) approaches yield comparable results ranging from 4.27 eV to 4.53 eV. The BHLYP approach yields BDEs that are all >1.6 eV below the experimental value, which is consistent with previous results for the multiple metal ligand bonds [39,97]. For the BLYP and BP86 approaches, the predicted ground state is now the $^4\Pi$, with BDEs that are somewhat higher than experiment, ranging from 5.05 eV to 5.32 eV and 5.16 eV to 5.45 eV, respectively. One possible explanation for discrepancies between experiment and theory is spin-orbit interactions, which are not explicitly included in the present calculations but were estimated above. The theoretical bond energies are calculated with respect to the average energy of all spin-orbit levels of the Os^+ (^{6}D) state, lying 0.363 eV above the $^6D_{9/2}$ ground state level, which is the appropriate asymptote for the experimental bond energy. For OsO^+ ($^6\Sigma^+$), there is no first-order spin-orbit splitting (although interactions with nearby levels could perturb this), such that corrected theoretical BDEs for this state should be decreased by 0.36 eV, as indicated in Table 4. Complicating the proper comparison between theory and experiment is the fact that the $^4\Pi$ state should exhibit first-order spin-orbit splitting, estimated above, such that the BDEs of the $^4\Pi$ state should be increased by 0.566–0.363 = 0.20 eV, as also shown in Table 4. (If the $^4\Phi$ state is the ground state, then the calculated BDEs should be lowered by 0.363–0.182 = 0.18 eV.) With this correction, all levels of theory now suggest that the bond energy measured experimentally is that of the $^4\Pi$ state, with BDEs calculated at the B3LYP and CCSD(*T*,full) levels being somewhat lower than experiment and those at the BLYP and BP86 levels somewhat higher than experiment, Table 4.

Additional doublet, quartet, and sextet excited states were also located at the B3LYP/def2-TZVPPD level of theory and are listed in Table 5. Variation of the orbital occupation in the $^4\Pi$ state led to another quartet state lying 0.05 eV higher in energy, but otherwise very similar bond length. This is similar to the behavior calculated by Ram et al. for the $^4\Pi$ and $^4\Phi$ states of OsN (where the calculated excitation energy is 0.22 eV) [94], hence we assign this other state as $^4\Phi$. Other states of OsO^+ located have excitation energies of 0.29–3.63 eV above the $^6\Sigma^+$, Table 5. It can be seen that most states identified as having bond orders of 2 have bond lengths of 1.71–1.77 Å. The $^2\Sigma^+$ and $^2\Delta$ states having bond orders of 3 decrease the bond length to ~1.6 Å, whereas the states with bond orders of 2.5 have intermediate bond lengths of 1.64–1.70 Å. Two states with bond orders of 1.5 have longer bonds, 1.79–1.86 Å. If the antibonding 3σ orbital is occupied, the bond lengths increase:

Table 5
Theoretical results for OsO^+ calculated at the B3LYP/def2-TZVPPD level of theory.

State	Configuration	Bond order	<s^2>	*r* (Os—O) (Å)	ω (cm^{-1})[a]	E_{rel} (eV)
$^6\Sigma^+$	$1\sigma^2 1\pi^4 1\delta^2 2\sigma^1 2\pi^2$	2	8.76	1.730	914	0.00
$^4\Pi$	$1\sigma^2 1\pi^4 1\delta^3 2\sigma^1 2\pi^1$	2.5	3.77	1.657	1035	0.02
$^4\Phi$	$1\sigma^2 1\pi^4 1\delta^3 2\sigma^1 2\pi^1$	2.5	3.77	1.656	1032	0.07
$^2\Sigma^+$	$1\sigma^2 1\pi^4 1\delta^4 2\sigma^1$	3	0.75	1.589	1167	0.29
$^2\Pi$	$1\sigma^2 1\pi^4 1\delta^4 2\pi^1$	2.5	1.60[b]	1.652	1051	0.51
$^2\Pi$	$1\sigma^2 1\pi^4 1\delta^3 2\sigma^1 2\pi^1$	2.5	1.77[b]	1.659	1028	0.51
$^2\Delta$	$1\sigma^2 1\pi^4 1\delta^3 2\sigma^2$	3	0.76	1.609	1097	0.69
$^4\Delta$	$1\sigma^2 1\pi^4 1\delta^3 2\pi^2$	2	4.44[b]	1.720	921	0.71
$^2\Pi$	$1\sigma^2 1\pi^4 1\delta^4 2\pi^1$	2.5	0.76	1.639	1087	0.80
$^2\Phi$	$1\sigma^2 1\pi^4 1\delta^3 2\sigma^1 2\pi^1$	2.5	1.75	1.654	1051	0.81
$^4\Sigma^+$	$1\sigma^2 1\pi^4 1\delta^2 2\sigma^1 2\pi^2$	2	4.76[b]	1.744	861	0.86
$^4\Delta$	$1\sigma^2 1\pi^4 1\delta^3 2\pi^2$	2	3.76	1.709	954	0.90
$^4\Pi$	$1\sigma^2 1\pi^4 1\delta^2 2\sigma^2 2\pi^1$	2.5	3.84	1.684	919	1.01
$^2\Delta$	$1\sigma^2 1\pi^4 1\delta^3 2\pi^2$	2	1.76[b]	1.714	934	1.41
$^4\Sigma^+$	$1\sigma^2 1\pi^4 1\delta^2 2\sigma^1 2\pi^2$	2	3.77	1.726	924	1.42
$^4\Delta$	$1\sigma^2 1\pi^4 1\delta^2 2\sigma^1 2\pi^2$	2	3.93	1.762	725	1.65
$^4\Gamma$	$1\sigma^2 1\pi^4 1\delta^2 2\sigma^1 2\pi^2$	2	3.76	1.731	902	2.05
$^2\Gamma$	$1\sigma^2 1\pi^4 1\delta^3 2\pi^2$	2	0.78	1.711	923	2.15
$^4\Delta$	$1\sigma^2 1\pi^4 1\delta^3 2\sigma^1 3\sigma^1$	2.5	3.84	1.697	883	2.92
$^6\Pi$	$1\sigma^2 1\pi^4 1\delta^2 2\sigma^1 2\pi^1 3\sigma^1$	2	9.12	1.833	587	2.94
$^4\Pi$	$1\sigma^2 1\pi^4 1\delta^2 2\pi^3$	1.5	3.79	1.789	790	3.04
$^4\Delta$	$1\sigma^2 1\pi^4 1\delta^1 2\sigma^2 2\pi^2$	2	3.76	1.765	846	3.22
$^8\Pi$	$1\sigma^2 1\pi^3 1\delta^2 2\sigma^1 2\pi^2 3\sigma^1$	1	15.76	2.116	447	3.39
$^6\Phi$	$1\sigma^1 1\pi^4 1\delta^3 2\sigma^1 2\pi^2$	1.5	8.76	1.860	690	3.63

[a] Calculated frequencies scaled by 0.989.
[b] Spin-contaminated.

Table 6
Theoretical results for $OOsO^+$ calculated at the B3LYP/def2-TZVPPD level of theory.[a]

State	Configuration	<s^2>	r (Os—O) (Å)	∠OOsO (°)	ω (cm^{-1})[b]	E_{rel} (eV)
$^2B_1$	$1a_1^2 1b_2^2 1a_2^2 2a_1^2 1b_1^2 2b_2^2 3a_1^2 2b_1^1$	0.94[c]	1.661	116.5	269, 965, 1065	0.00
$^4B_1$	$1a_1^2 1b_2^2 1a_2^2 2a_1^2 1b_1^2 2b_2^2 3a_1^1 2b_1^1 4a_1^1$	3.75	1.678	126.6	296, 962, 1030	0.23
$^2A_1$	$1a_1^2 1b_2^2 1a_2^2 2a_1^2 1b_1^2 2b_2^2 3a_1^1 2b_1^2$	0.76	1.670	124.2	296, 983, 1056	0.24
$^4B_2$	$1a_1^2 1b_2^2 1a_2^2 2a_1^2 1b_1^2 2b_2^2 3a_1^1 2b_1^1 2a_2^1$	3.76	1.697 (1.697)	104.5 (104.7)	369, 921, 999	0.61 (0.00)
$^2A_1$	$1a_1^2 1b_2^2 1a_2^2 2a_1^2 1b_1^2 2b_2^2 3a_1^2 4a_1^1$	0.76	1.668	114.6	300, 973, 1046	0.80
$^2A_2$	$1a_1^2 1b_2^2 1a_2^2 2a_1^2 1b_1^2 2b_2^2 3a_1^2 2a_2^1$	0.87	1.682 (1.681)	99.5 (99.7)	388, 1003, 1017	1.34 (0.66)
$^4A_2$	$1a_1^2 1b_2^2 1a_2^2 2a_1^2 1b_1^2 2b_2^2 3a_1^1 4a_1^1 2a_2^1$	3.79	1.710	104.4	320, 947, 952	1.90
$^6A_1$	$1a_1^2 1b_2^2 1a_2^2 2a_1^2 1b_1^2 2b_2^1 3a_1^1 2b_1^1 4a_1^1 2a_2^1$	8.77	1.782	95.4	147, 555, 858	1.91 (1.27)
$^4A_2$[d]	$1a_1^2 1b_2^2 1a_2^2 2a_1^2 1b_1^2 2b_2^1 3a_1^2 2b_1^1 4a_1^1$	3.76	1.705	147.6	247i, 107, 947	1.97
$^2B_2$ ($^2\Sigma^+$)	$1a_1^2 1b_2^2 1a_2^2 2a_1^2 1b_1^2 2b_2^1 3a_1^2 2b_1^2$	1.48[c]	1.697	180.0	94, 562, 978	2.10
$^6A''$ ($^6A_2$)	$1a_1^2 1b_2^2 1a_2^2 2a_1^2 1b_1^1 2b_2^2 3a_1^1 2b_1^1 4a_1^1 2a_2^1$	8.76	1.717, 1.905	126.4	201, 586, 891	2.68
$^2A_2$	$1a_1^2 1b_2^2 1a_2^2 2a_1^2 1b_1^2 2b_2^1 3a_1^2 2b_1^1 4a_1^1$	1.76[c]	1.702	156.5	114, 283, 963	2.82
$^4A_2$	$1a_1^2 1b_2^2 1a_2^2 2a_1^2 1b_1^2 2b_2^2 3a_1^1 2b_1^1 3b_2^1$	3.76	1.735	121.8	250, 783, 939	2.87
$^2A_2$	$1a_1^2 1b_2^2 1a_2^2 2a_1^2 1b_1^2 2b_2^2 3a_1^1 2b_1^1 3b_2^1$	1.82[c]	1.743	121.0	250, 699, 884	3.26
$^6A''$ ($^6\Delta$)[e]	$1a_1^2 1b_2^2 1a_2^2 2a_1^1 1b_1^2 2b_2^2 3a_1^1 2b_1^1 4a_1^1 3b_2^1$	8.78	1.778, 1.879	180.0	233i, 194i, 203, 824	3.27
$^2B_2$	$1a_1^2 1b_2^2 1a_2^2 2a_1^2 1b_1^2 2b_2^2 3a_1^2 3b_2^1$	0.79	1.720	112.1	268, 840, 963	3.36
$^6B_2$	$1a_1^2 1b_2^2 1a_2^2 2a_1^1 1b_1^2 2b_2^2 3a_1^1 2b_1^1 4a_1^1 2a_2^1$	8.83	1.799	135.9	209, 717, 803	3.42
$^4B_2$	$1a_1^2 1b_2^2 1a_2^2 2a_1^2 1b_1^2 2b_2^2 3a_1^1 4a_1^1 3b_2^1$	4.87[c]	1.828	148.2	124, 497, 743	3.49
$^6B_1$	$1a_1^2 1b_2^2 1a_2^1 2a_1^2 1b_1^2 2b_2^2 3a_1^1 2b_1^1 4a_1^1 2a_2^1$	8.77	1.826	102.9	209, 784, 1583	3.70
$^6B_1$	$1a_1^2 1b_2^2 1a_2^2 2a_1^2 1b_1^2 2b_2^1 3a_1^1 2b_1^1 4a_1^1 3b_2^1$	8.77	1.776	156.1	136, 850, 3496	3.79
$^6B_2$[d]	$1a_1^2 1b_2^2 1a_2^2 2a_1^2 1b_1^2 2b_2^1 2a_2^1 3a_1^1 2b_1^1 3b_2^1$	8.88	1.832	103.5	255i, 181, 760	4.10
$^8A''$ ($^8A_2$)	$1a_1^2 1b_2^2 1a_2^2 2a_1^2 1b_1^1 2b_2^1 2a_2^1 3a_1^1 2b_1^1 3b_2^1 4a_1^1$	15.77	1.737, 2.566	82.3	82, 195, 893	4.56
$^4A_1$	$1a_1^2 1b_2^2 1a_2^2 2a_1^2 1b_1^2 2b_2^2 2b_1^1 2a_2^1 3b_2^1$	3.82	1.788	111.1	251, 608, 797	4.93

[a] Values in parentheses are from [14].
[b] Calculated frequencies scaled by 0.989.
[c] Spin-contaminated.
[d] Stable only at C_{2v} symmetry. Has an imaginary asymmetric stretch.
[e] Stable only at 180° and C_{2v}. Has an imaginary bend and asymmetric stretch.

compare $^4\Phi$ and $^4\Delta$ with an increase of 0.04 Å and $^6\Sigma^+$ and $^6\Pi$ with an increase of 0.10 Å. We also searched for the lowest energy octet state, locating the $^8\Pi$ at 3.39 eV above the ground state. Not surprisingly, this state has a bond order of only 1 such that the bond length extends to 2.12 Å. Examination of the vibrational frequencies find that they also track reasonably well with the bond order, ~1130 cm^{-1} for 3, ~1050 cm^{-1} for 2.5, ~900 cm^{-1} for 2, ~740 cm^{-1} for 1.5, and 450 cm^{-1} for 1 with the greatest exceptions again associated with occupation of the 3σ mo. Finally, although these calculations should provide useful guidelines for the presence of excited states, they are limited to single configurations and therefore do not address the true multiconfiguration character of these states, as nicely illustrated by the CMRCI calculations of Ram et al. on the isoelectronic OsN molecule [94].

3.4. Analysis of the OsO_2^+ cross section

As discussed above, the OsO_2^+ product is formed in the secondary reaction (2). This process appears to be barrierless, as shown in Fig. 2. Thus, these results indicate that $D_0(OOs^+—O) > D_0(O—O) = 5.115$ eV. This agrees with the 5.4 ± 0.7 eV value obtained from appearance energy determinations by Watson et al. [16], but not that of Dillard and Kiser, 4.1 ± 0.3 eV [15]. Irikura and Beauchamp assigned this BDE as 4.57 ± 0.52 eV, with an upper limit of 5.09 eV determined on the basis of observing the reaction $OsO_2^+ + H_2 \rightarrow OsO^+ + H_2O$ (20% efficiency) [13]. Given this efficiency, it is possible that only excited states (vibrational or electronic) actually undergo this reaction, such that these results are probably consistent as long as $D_0(OOs^+—O)$ is close to 5.1 eV. This is consistent with the theoretical results described in the next section.

3.5. Theoretical results for OsO_2^+

In previous theoretical work on OsO_2^+, Jiang et al. located a ground state quartet with doublet and sextet states lying 0.66 eV and 1.27 eV, respectively, higher in energy [14]. Wang et al. found that a quartet (unspecified geometry) is the ground state, although it is not apparent whether doublet spin species were examined [22]. For OsO_2^+, our calculations predict the ground state to be $^2B_1$, with equal Os—O bond lengths of 1.661 Å and a bond angle of 116.5°, Table 6. The valence electronic configuration of this state is $1a_1^2 1b_2^2 1a_2^2 2a_1^2 1b_1^2 2b_2^2 3a_1^2 2b_1^1$. The bonding in metal dioxides has been described previously by Kretzschmar et al. (although they use x as the symmetry axis with the molecule in the xz plane, such that b_1 (out-of-plane) and b_2 (in-plane) designations are switched compared with the nomenclature adopted here) [98]. Here, we utilize the conventions recommended previously [99], in which the molecule has C_{2v} symmetry along the z-axis with the molecule lying in the yz plane. Core electrons on Os (5s, 5p) and O (1s, 2s) are not included in these mos. The $1a_1$ orbital is bonding and formed from the $5d_y^2$ orbital of Os and the $2p_z$ of each oxygen atom, thus forming in-plane Os—O π bonds. There are two doubly occupied, σ-bonding mos ($1b_2$ and $2a_1$) resulting from interaction of the Os($5d_{yz}$) and Os($5d_{x^2-z^2}$) orbitals with in-phase and out-of-phase combinations of the O($2p_y$) orbitals on each oxygen atom. The $1a_2$ and $1b_1$ mos are doubly occupied out-of-plane π-like mos, which involve the Os($5d_{xy}$) and Os($5d_{xz}$) orbitals combined with out-of-phase and in-phase combinations of the O($2p_x$) orbitals, respectively. The $2b_2$ mo, which is mostly nonbonding in character, is formed from an out-of-phase combination of O($2p_z$) orbitals. The $3a_1$ orbital, also largely nonbonding, is a 6s-$5d_{x^2}$ hybrid along with a little O($2p_y$) character. Higher lying mos include $2b_1$, $4a_1$, $2a_2$, $3b_2$, and $5a_1$, which are antibonding versions of the $1b_1$, $2a_1$, $1a_2$, $1b_2$, and $1a_1$ bonding mos, respectively. From this, the $^2B_1$ state has 10 electrons in bonding and 1 electron in antibonding mos such that each Os—O bond has a bond order of 2.25. This is reasonable when one compares the 1.661 Å bond length for each Os—O bond in the $^2B_1$ state with those listed for the OsO^+ species having bond orders of 2.5, Table 5. Further, this bond order characterization is commensurate with the bond energy. At the B3LYP/def2-TZVPPD level of theory, the $^2B_1$ state is calculated to lie 4.27 eV below the Os^+ (^6D) + O_2 reactant asymptote and to have a $D_0(OOs^+—O)$ BDE of 5.06 eV. This theoretical value compares favorably to the experimental limits of >5.12 eV (measured here) and <5.09 eV (measured previously) [13].

Table 7
Theoretical results for $Os^+(O_2)$ calculated at the B3LYP/def2-TZVPPD level of theory.

State	Configuration	<s^2>	r (Os—O) (Å)	r (O—O) (Å)	∠OOsO (°)	ω (cm^{-1})[a]	E_{rel} (eV)[b]
$^4B_2$	$1a_1^2 1b_2^2 1a_2^2 2a_1^2 1b_1^2 3a_1^2 2b_1^1 4a_1^1 2a_2^1$	3.77	1.862	1.416	44.7	594, 600, 987	3.11
$^4A_2$	$1a_1^2 1b_2^2 1a_2^2 2a_1^2 1b_1^2 3a_1^1 2b_1^2 4a_1^1 2a_2^1$	3.77	1.912	1.348	41.3	212, 535, 1046	3.38
$^2A_1$	$1a_1^2 1b_2^2 1a_2^2 2a_1^2 1b_1^2 3a_1^2 2b_1^2 4a_1^1$	1.51[c]	1.958	1.289	38.4	391, 473, 1220	3.41
$^2B_1$	$1a_1^2 1b_2^2 1a_2^2 2a_1^2 1b_1^2 3a_1^2 2b_1^1 4a_1^2$	1.39[c]	1.919	1.310	39.9	357, 432, 1164	3.57
$^4A''$	$1a'^2 2a'^2 1a''^2 3a'^2 2a''^2 4a'^2 5a'^1 3a''^1 6a'^1$	4.46[c]	1.880, 2.689	1.264	24.9	166, 555, 1171	3.62
$^6A'$	$1a'^2 2a'^2 1a''^2 3a'^2 2a''^2 4a'^1 5a'^1 3a''^1 4a''^1 6a'^1$	8.76	1.908, 2.271	1.311	35.2	254, 586, 1104	3.63
$^4A'$	$1a'^2 2a'^2 1a''^2 3a'^2 2a''^2 4a'^1 5a'^1 3a''^2 6a'^1$	4.47[c]	1.877, 2.737	1.258	23.4	159, 494, 1193	3.65
$^6A_1$[d]	$1a_1^2 1b_2^2 1a_2^2 2a_1^2 1b_1^2 2b_2^1 3a_1^1 2b_1^1 4a_1^1 2a_2^1$	8.76	2.022	1.363	39.4	1053i, 353, 1038	3.88
$^2A''$	$1a'^2 2a'^2 1a''^2 3a'^2 2a''^2 4a'^2 5a'^2 3a''^1$	2.10[c]	1.859, 2.883	1.225	16.7	188, 408, 1375	3.90
$^2A'$	$1a'^2 2a'^2 1a''^2 3a'^2 2a''^2 4a'^2 5a'^1 3a''^2$	2.05[c]	1.846, 2.895	1.225	15.7	185, 409, 1366	3.92
$^6A''$	$1a'^2 2a'^2 1a''^2 3a'^2 2a''^1 4a'^2 5a'^1 3a''^1 4a''^1 6a'^1$	8.76	1.953, 2.510	1.292	30.5	143, 570, 1103	4.05
$^6B_2$	$1a_1^2 1b_2^2 1a_2^2 2a_1^2 1b_1^2 3a_1^1 2b_1^1 4a_1^1 2a_2^1 5a_1^1$	8.80	2.006	1.297	37.7	332, 1171, 1291	4.38

[a] Calculated frequencies scaled by 0.989.
[b] Energy relative to the OsO_2^+ ($^2B_1$) state of Table 6.
[c] Spin-contaminated.
[d] Stable only at C_{2v} symmetry. Has an imaginary asymmetric stretch.

Table 6 lists the geometries and energies of various stable states of osmium dioxide cations, $OOsO^+$, calculated at the B3LYP/def2-TZVPPD level of theory. The first excited state of OsO_2^+ is calculated to be a $^4B_1$ state lying 0.23 eV above the ground state and having an Os^+—O bond length of 1.678 Å and an angle of 126.6°. This state is formed by moving an electron from the $3a_1$ to the $4a_1$ orbital. The $^2A_1$ state, nearly isoenergetic with the $^4B_1$, has an Os^+—O bond length of 1.670 Å and an angle of 124.2° and is formed by a $3a_1$ to $2b_1$ excitation. Other excited states with C_{2v} symmetry were located with excitation energies of 0.61–4.93 eV above the ground state, bond lengths of 1.67–1.83 Å, and bond angles of 95.4°–180.0°. The $^4B_2$, $^2A_2$, and $^6A_1$ are the states previously located by Zhang et al. [14], identified on the basis of the nearly identical geometries and excitation energies, Table 6. Of the states we located, only one is linear, at 2.10 eV above the ground state. In C_{2v} symmetry, this state has a $^2B_2$ designation but is $^2\Sigma^+$ in $C_{\infty v}$ symmetry with a $1\sigma^2 1\pi^4 2\pi^4 2\sigma^1 1\delta^4$ orbital occupation. It can also be noted that the $^4A_2$ state at 1.97 eV and the $^6B_2$ state at 4.10 eV are stable only if C_{2v} symmetry is maintained, because these states have imaginary asymmetric stretches that permit them to collapse to the lower lying $^4B_1$ and $^6A_1$ states, respectively. Finally, two related $^6A''$ states were located having only C_s symmetry, such that the two Os—O bonds are different lengths. The $^6A''$ state at 2.68 eV is given in Table 6 with its orbital occupancy indicated by the C_{2v} symmetry equivalents. As this state bends toward linearity, it becomes degenerate with the other $^6A''$ state, which has a minimum at 180°, where it becomes a $^6\Delta$ state with a $1\sigma^2 1\pi^4 2\pi^3 2\sigma^2 1\delta^2 3\sigma^1 3\pi^1$ orbital occupation. Thus, the $^6\Delta$ state has an imaginary frequency (a bend), such that it collapses to the lower $^6A''$ state. We also located the lowest energy octet state, $^8A''$, which is strongly distorted with one

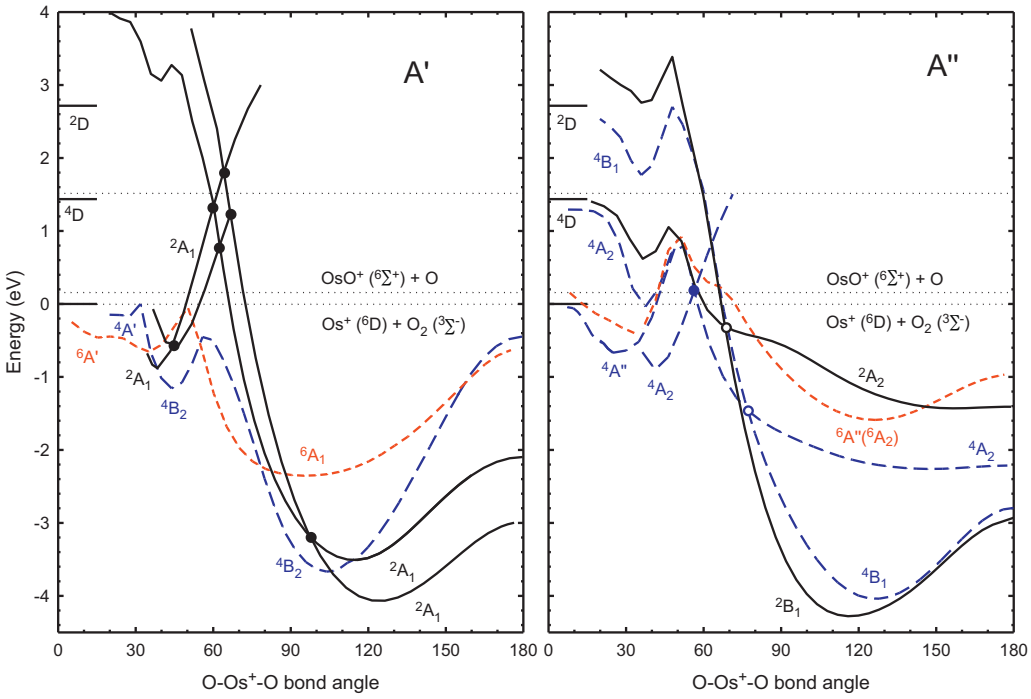

Fig. 4. B3LYP/def2-TZVPPD calculations of the potential energy surfaces for the interaction of Os^+ with O_2 in C_{2v} symmetry as a function of the O—Os^+—O bond angle in degrees. The surfaces are separated into A′ (part a) and A″ (part b) symmetry with doublet, quartet, and sextet states indicated by black full, blue long dashed, and red short dashed lines, respectively. Horizontal dotted lines indicate the experimental energy zero, corresponding to the Os^+ (^6D) + O_2 ($^3\Sigma^-$) reactants at 0.0 eV, and the two experimental energy thresholds determined for formation of OsO^+ + O products, 0.16 and 1.52 eV above the reactants. Circles indicate avoided crossings in C_{2v} (filled) and C_s (open) symmetry.

short, 1.737 Å, and one long, 2.566 Å, Os—O bond. As expected, such a high spin state lies quite high in energy such that octet surfaces were not explored.

In addition to this set of osmium dioxide cation states, there are also a number of states best characterized as adducts of Os^+ with O_2. These are collected in Table 7 and are typified by small OOsO bond angles (<45°), short OO bond distances (1.22–1.42 Å compared to free O_2 at 1.204 Å), and larger Os—O bond lengths (1.85–2.02 Å) than the dioxides. Half of these states retain C_{2v} symmetry, whereas the others are bent such that the two Os—O bond lengths are unequal. All are stable except for the $^6A_1$ state, which has in imaginary asymmetric stretch such that it collapses to the $^6A'$ state. All of these states, except the highest lying $^6B_2$ are bound relative to the Os^+ (^6D) + O_2 reactants and can be viewed as the complexes formed in the entrance channel of the $Os^+ + O_2$ reactants.

3.6. Potential energy surfaces for $Os^+ + O_2$ on the way to forming $OsO^+ + O$

Calculated potential energy surfaces for the interaction of Os^+ with O_2 ($^3\Sigma_g^-$) are shown in Fig. 4. They are separated into surfaces having A″ and A″ symmetry as only curves within these groups will strongly interact under experimental conditions for this triatomic system, which necessarily has a plane of symmetry. In most cases, species have C_{2v} symmetry throughout. In the interaction between Os^+ (^6D) with O_2 ($^3\Sigma_g^-$), the first step is formation of association complex intermediates, $Os^+(O_2)$ ($^4B_2$) on the A′ surfaces and $Os^+(O_2)$ ($^4A_2$) on the A″ surfaces, which have energies 1.16 eV and 0.89 eV below the Os^+ (^6D) + O_2 ($^3\Sigma_g^-$) asymptote. The former intermediate has OsO bond lengths of 1.862 Å, a bond angle of 44.7°, and a valence electron configuration of $1a_1^2 1b_2^2 1a_2^2 2a_1^2 1b_1^2 3a_1^2 2b_1^1 4a_1^1 2a_2^1$. The latter intermediate excites an electron from the $3a_1$ to the $2b_1$ mo and extends the bonds to 1.912 Å. As the OOsO bond angle gets larger, the potential energy surfaces evolve into the more strongly bound osmium dioxide cationic species, with the $^2A_1$ and $^2B_1$ states being the lowest in energy on the A′ and A″ surfaces. Note that doublet states of OsO_2^+ cannot be formed in spin-allowed processes from the ground state Os^+ (^6D) + O_2 ($^3\Sigma_g^-$) reactants and therefore can only be accessed by a curve crossing with one of the quartet or sextet surfaces. Importantly, all of the OsO_2^+ surfaces have minima that lie below the $OsO^+ + O$ product asymptote, calculated to be 0.80 eV (0.62 eV including estimated spin-orbit energies) above the $Os^+ + O_2$ asymptote at this level of theory (0.16 eV experimentally). Using the CCSD(*T*,full)/def2-QZVPPD approach, the calculated endothermicity is 0.59 eV (0.49 eV including estimated spin-orbit energies).

Formation of OsO^+ ($^6\Sigma^+$) + O (^3P) products can evolve in spin-allowed pathways from any of the quartet or sextet species and OsO^+ ($^4\Pi/\Phi$) + O (^3P) can be formed from doublet, quartet, and sextet intermediates. These dissociation pathways require breaking C_{2v} symmetry such that they are not conveniently shown in Fig. 4. The observation that the thresholds for formation of OsO^+ in the reaction of Os^+ with O_2 are consistent with the thermochemistry determined in the literature indicates that there are no barriers in excess of the endothermicity of the reaction, consistent with the qualitative character of the lowest energy PESs shown in Fig. 4. Furthermore, explicit calculations of the surfaces for OOs^+—O bond cleavage from the four lowest OsO_2^+ states show no reverse activation barriers.

4. Discussion

The behavior observed for reaction (1), Fig. 1, is unusual in that two endothermic features are observed and the first declines well before the onset of reaction (4). Several plausible explanations are discussed here, although it will be seen that none appear to be definitive.

1) One potential explanation for the two features is the presence of excited states of Os^+. We discount this possibility because no evidence for such excited states is observed in other systems, reactions with H_2 [53] and CH_4. Further, addition of a quenching gas (N_2O) to the source region yielded no change in the cross sections observed.
2) The high energy feature could correspond to formation of ground state O (^3P) at low energies and O (^1D) at high energies. However, the excitation energy of 1.36 ± 0.11 eV measured here is well below the 1.97 eV associated with this excitation [91].
3) On the basis of a comparison with previous results for reactions of $V^+ + CS_2$ [92], this behavior is plausibly assigned to an overall spin-forbidden reaction at low energy and an overall spin-allowed process at high energies, thus forming two different electronic states of the OsO^+ product ion. This would potentially explain the appearance of two features as well as the rapid decline in the first feature at low energies. Belying this explanation is the fact that both reactions (9) and (10) are spin-allowed.

$$Os^+(^6D) + O_2(^3\Sigma_g^-) \rightarrow OsO^+(^6\Sigma^+) + O(^3P) \quad (9)$$

$$Os^+(^6D) + O_2(^3\Sigma_g^-) \rightarrow OsO^+(^4\Pi/\Phi) + O(^3P) \quad (10)$$

such that formation of ground state products (no matter what their identity) from ground state reactants is spin-allowed. Indeed, formation of any OsO^+ product state is spin-allowed, as even doublet states of OsO^+ can be formed via quartet intermediates. Furthermore, it seems unlikely that spin is a very good quantum number for this heavy element system. Nevertheless, we can pursue this idea further by comparing the experimental excitation energy of 1.36 ± 0.11 eV with the theoretical excitation energies in Table 5. At this energy, there is both a $^2\Delta$ state at 1.41 eV and a $^4\Sigma^+$ state at 1.42 eV, with alternatives ≥0.2 eV farther off. There is nothing to indicate that either of these states is unique, in that there are both $^2\Delta$ and $^4\Sigma^+$ states at lower energy as well as states having the same orbital configurations. It should also be noted that a unique state assignment of this energy is also complicated by the spin-orbit interactions discussed above, as these will alter the calculated excitation energies, such that several spin-orbit levels of multiple states could lie at 1.36 eV.
4) In the S^+ (^4S) + H_2 ($^1\Sigma_g^+$) reaction system, analogous behavior to that observed here was also found and correlated with spin-forbidden (along a low-energy doublet surface) and spin-allowed (along a high-energy quartet surface) pathways that ultimately formed the same ground state SH^+ ($^3\Sigma^-$) + H (^2S) products [93]. In this scenario, $Os^+ + O_2$ would react at low collision energies to form the ground state OsO_2^+ ($^2B_1$) intermediate or perhaps the low-lying OsO_2^+ ($^2A_1$), which are technically spin-forbidden processes. These intermediates could then dissociate to form either OsO^+ ($^4\Pi/\Phi$) in a spin-allowed process or OsO^+($^6\Sigma^+$) by crossing to a quartet surface in the exit channel. As the energy increases, the coupling to the doublet surface associated with these intermediates would be reduced, explaining the early decline in the first cross section feature. It is not obvious, however, why these same products cannot be formed from other low-lying states of OsO_2^+, both quartets and sextets, that can be formed in spin-allowed processes. Furthermore, this scenario does not provide a clear explanation for the origins of the higher energy cross section feature.
5) An intriguing possibility focuses on the character of the surfaces in the entrance channel, which is effectively shown in Fig. 4 at

small OOsO bond angles. For surfaces of A′ symmetry (which should account for 3/5 of all surfaces evolving from ground state reactants), it can be seen that the ground state reactants have low-energy pathways to the stable OsO_2^+ intermediates along both the $^6A'$ and $^4A'/^4B_2$ surfaces. Along these surfaces, there are no barriers to form OsO_2^+ in excess of the reactant energy. Likewise, there should be no barriers for dissociation to $OsO^+ + O$ in excess of the product asymptotic energy. Thus, at low kinetic energies, the reactants pass slowly through the crossing regions, allowing the electrons to adjust to different configurations along the reaction coordinate. Under such conditions, spin inversion can be efficient, and adiabatic behavior is expected. However, all of these surfaces exhibit avoided crossings with surfaces evolving from higher energy reactant states, such that as the nuclear motion speeds up at elevated collision energies, the reactants pass more quickly through the crossing regions, the electrons have less time to adapt, and the Born–Oppenheimer approximation begins to fail. Thus, as the kinetic energy of the reactants increases, it becomes increasingly likely that the reactants will behave diabatically during the collision event and remain on the surface associated with the electron configuration of the ground state reactants. This would lead to a higher barrier to the reaction, observed experimentally as the second cross section feature. Intriguingly, the surfaces of A″ symmetry (which should account for 2/5 of all surfaces evolving from ground state reactants) are qualitatively different in the entrance channel. Here, no low-energy pathways were found, such that all the surfaces exhibit some type of barrier as the reactants approach. Thus, one possibility is that the low energy behavior observed experimentally corresponds to reactions along the A′ surfaces, which then shut off as the energy gets higher, perhaps because of diabatic behavior. The high energy feature observed experimentally could then be associated with reactions along the A″ surfaces with possible contributions from diabatic pathways on A′.

Clearly, none of these explanations is particularly satisfying, although it seems clear that the explanation for the observed experimental behavior must be some type of adiabatic behavior at low energies followed by nonadiabatic behavior at higher energies. We find it particularly interesting that such behavior is observed for this heavy metal system where spin is no longer likely to be a very good quantum number. If so, then there should be efficient coupling between the doublet, quartet, and sextet surfaces shown in Fig. 4, such that the reaction is controlled by effects in the entrance channel.

5. Conclusion

The kinetic-energy dependence of $Os^+ + O_2$ reaction is examined using guided ion beam mass spectrometry. The cross section for OsO^+ formation exhibits distinct endothermic features with thresholds measured to be 0.16 ± 0.02 eV and 1.52 ± 0.11 eV. The former threshold yields a bond energy for OsO^+ of 4.96 ± 0.02 eV, which agrees well with previous approximate experimental values. Formation of OsO_2^+ was also observed in an exothermic secondary process, leading to thermochemistry in reasonable agreement with the literature.

Detailed quantum mechanical calculations are also performed for OsO^+ and OsO_2^+ species. The nature of the bonding is analyzed at the B3LYP, BHLYP, BLYP, BP86, and CCSD(*T*,full) levels of theory. Basis sets for the metal include def2-QZVPPD, def2-TZVPPD, SDD, and HW+, while the def2 basis sets and 6-311G+(3df) were used for oxygen. Reasonable agreement between theoretical and experimental bond energies is found for most levels of theory, with B3LYP and CCSD(*T*,full) being on the low side and BLYP and BP86 being on the high side and BHLYP performing rather poorly. The calculated ground state of OsO^+ is either $^6\Sigma^+$ or $^4\Pi/\Phi$, although additional consideration of spin-orbit effects and comparison with the isoelectronic OsN molecule suggests that the $^4\Pi$ is the probable ground state. Potential energy surfaces for the interaction of Os^+ with O_2 are also calculated at the B3LYP/def2-TZVPPD level of theory. These surfaces demonstrate that Os^+ inserts into O_2 to form ground state OsO_2^+ via a curve crossing model and that ground state OsO^+ can be formed with no barriers in excess of endothermicity, consistent with the experimental results.

Several possible reasons for the unusual behavior observed here are explored, but no completely satisfying explanation evolves. It seems clear that this heavy metal system exhibits both adiabatic behavior at low collision energy followed by nonadiabatic behavior at higher energies, but the detailed nature of the nonadiabatic behavior is not evident.

Acknowledgements

This research is funded by the National Science Foundation, CHE-1049580. Laura Parke is thanked for helping to develop the safety precautions needed to handle osmium safely. Professor Michael D. Morse is thanked for the osmium sample used in these experiments and for several very helpful discussions.

References

[1] J.F. Harrison, Chemical Reviews 100 (2000) 679.
[2] A.J. Bridgeman, J. Rothery, Journal of the Chemical Society. Dalton Transactions (2000) 211.
[3] G.L. Gutsev, L. Andrews, C.W. Bauchlicher Jr., Theoretical Chemistry Accounts 109 (2003) 298.
[4] P.E.M. Siegbahn, Chemical Physics Letters 201 (1993) 15.
[5] F.A. Cotton, G. Wilkinson, Advanced Inorganic Chemistry, Wiley, New York, 1988.
[6] H. Schwarz, D. Schröder, Pure and Applied Chemistry 72 (2000) 2319.
[7] K.K. Irikura, J.L. Beauchamp, Journal of the American Chemical Society 113 (1991) 2769.
[8] K.K. Irikura, J.L. Beauchamp, Journal of Physical Chemistry 95 (1991) 8344.
[9] H. Schwarz, Angewandte Chemie International Edition (English) 30 (1991) 820.
[10] J.C. Weisshaar, Accounts of Chemical Research 26 (1993) 213.
[11] D. Schröder, H. Schwarz, Angewandte Chemie International Edition (English) 34 (1995) 1973.
[12] D. Schröder, H. Schwarz, S. Shaik, Structure and Bonding 97 (2000) 91.
[13] K.K. Irikura, J.L. Beauchamp, Journal of the American Chemical Society 111 (1989) 75.
[14] G. Zhang, S. Li, Y. Jiang, Organometallics 23 (2004) 3656.
[15] J.G. Dillard, R.W. Kiser, Journal of Physical Chemistry 69 (1965) 3893.
[16] L.R. Watson, T. Thiem, R.A. Dressler, R.H. Salter, E. Murad, Journal of Physical Chemistry 93 (1991) 8944.
[17] G.K. Koyanagi, D. Caraiman, V. Blagojevic, D.K. Bohme, Journal of Physical Chemistry A 106 (2002) 4581.
[18] U. Rieth, A. Herlert, J.V. Kratz, L. Schweikhard, M. Vogel, C. Walther, Radiochimica Acta 90 (2002) 337.
[19] G. Marx, A. Dretzke, A. Herlert, W. Lauth, H. Backe, L. Schweikhard, International Journal of Mass Spectrometry 242 (2005) 87.
[20] C. Yao, W. Guan, P. Song, Z.M. Su, J.D. Feng, L.K. Yan, Z. Wu, Journal of Theoretical Chemistry Accounts 117 (2007) 115.
[21] T.H. Li, C.M. Wang, S.W. Yu, X.Y. Liu, H. Fu, X.G. Xie, Chinese Chemical Letters 20 (2009) 1010.
[22] Y.-C. Wang, Q. Wang, Z.-Y. Geng, L.-L. Lv, X.-B. Wang, H.-W. Liu, Q. Wang, D.-D. Cui, Chemical Physics Letters 498 (2010) 245.
[23] N. Aristov, P.B. Armentrout, Journal of Physical Chemistry 90 (1986) 5135.
[24] S.K. Loh, E.R. Fisher, L. Lian, R.H. Schultz, P.B. Armentrout, Journal of Chemical Physics 91 (1989) 3159.
[25] S.K. Loh, L. Lian, P.B. Armentrout, Journal of Chemical Physics 91 (1989) 6148.
[26] E.R. Fisher, J.L. Elkind, D.E. Clemmer, R. Georgiadis, S.K. Loh, N. Aristov, L.S. Sunderlin, P.B. Armentrout, Journal of Chemical Physics 93 (1990) 2676.
[27] D.E. Clemmer, J.L. Elkind, N. Aristov, P.B. Armentrout, Journal of Chemical Physics 95 (1991) 3387.
[28] D.E. Clemmer, N.F. Dalleska, P.B. Armentrout, Journal of Chemical Physics 95 (1991) 7263.
[29] D.E. Clemmer, N.F. Dalleska, P.B. Armentrout, Chemical Physics Letters 190 (1992) 259.
[30] M.R. Sievers, P.B. Armentrout, Journal of Chemical Physics 102 (1995) 754.
[31] M.T. Rodgers, B. Walker, P.B. Armentrout, International Journal of Mass Spectrometry 182–183 (1999) 99.

[32] Y.-M. Chen, P.B. Armentrout, Journal of Chemical Physics 103 (1995) 618.
[33] M.R. Sievers, Y.-M. Chen, P.B. Armentrout, Journal of Chemical Physics 105 (1996) 6322.
[34] M.R. Sievers, P.B. Armentrout, International Journal of Mass Spectrometry 179–180 (1998) 103.
[35] M.R. Sievers, P.B. Armentrout, Journal of Physical Chemistry A 102 (1998) 10754.
[36] M.R. Sievers, P.B. Armentrout, Inorganic Chemistry 38 (1999) 397.
[37] M.R. Sievers, P.B. Armentrout, International Journal of Mass Spectrometry 185–187 (1999) 117.
[38] C.S. Hinton, F.-X. Li, P.B. Armentrout, International Journal of Mass Spectrometry 280 (2009) 226.
[39] C.S. Hinton, M. Citir, M. Manard, P.B. Armentrout, International Journal of Mass Spectrometry 308 (2011) 265.
[40] X.-G. Zhang, P.B. Armentrout, Journal of Physical Chemistry A 107 (2003) 8904.
[41] X.-G. Zhang, P.B. Armentrout, Journal of Physical Chemistry A 107 (2003) 8915.
[42] F.-X. Li, K. Gorham, P.B. Armentrout, Journal of Physical Chemistry A 114 (2010) 11043.
[43] M.E. Weber, J.L. Elkind, P.B. Armentrout, Journal of Chemical Physics 84 (1986) 1521.
[44] D.E. Clemmer, M.E. Weber, P.B. Armentrout, Journal of Physical Chemistry 96 (1992) 10888.
[45] N.F. Dalleska, P.B. Armentrout, International Journal of Mass Spectrometry and Ion Processes 134 (1994) 203.
[46] S.K. Loh, D.A. Hales, L. Lian, P.B. Armentrout, Journal of Chemical Physics 90 (1989) 5466.
[47] R.H. Schultz, P.B. Armentrout, International Journal of Mass Spectrometry 107 (1991) 29.
[48] E. Teloy, D. Gerlich, Chemical Physics 4 (1974) 417.
[49] D. Gerlich, Advanced Chemical Physics 82 (1992) 1.
[50] N.R. Daly, Review of Scientific Instruments 31 (1960) 264.
[51] K.M. Ervin, P.B. Armentrout, Journal of Chemical Physics 83 (1985) 166.
[52] P.J. Chantry, Journal of Chemical Physics 55 (1971) 2746.
[53] C.S. Hinton, M. Citir, P.B. Armentrout, Journal of Chemical Physics 135 (2011) 234302.
[54] B.L. Kickel, P.B. Armentrout, Journal of the American Chemical Society 117 (1995) 4057.
[55] D.E. Clemmer, Y.-M. Chen, F.A. Khan, P.B. Armentrout, Journal of Physical Chemistry 98 (1994) 6522.
[56] C.L. Haynes, P.B. Armentrout, Organometallics 13 (1994) 3480.
[57] B.L. Kickel, P.B. Armentrout, Journal of the American Chemical Society 117 (1995) 764.
[58] Y.-M. Chen, J.L. Elkind, P.B. Armentrout, Journal of Physical Chemistry 99 (1995) 10438.
[59] M.R. Sievers, Y.-M. Chen, J.L. Elkind, P.B. Armentrout, Journal of Physical Chemistry 100 (1996) 54.
[60] C.E. Moore, Atomic energy levels, National Standard Reference Data Series, Vol. 3, U.S., National Bureau Standard, 1971, pp. 35.
[61] T.A.M. Van Kleef, P.F.A. Klinkenberg, Physica 27 (1961) 83.
[62] P.B. Armentrout, International Journal of Mass Spectrometry 200 (2000) 219.
[63] W.J. Chesnavich, M.T. Bowers, Journal of Physical Chemistry 83 (1979) 900.
[64] P.B. Armentrout, in: N.G. Adams, L.M. Babcock (Eds.), Advances in Gas Phase Ion Chemistry, Vol. 1, JAI, Greenwich, 1992, p. 83.
[65] F. Muntean, P.B. Armentrout, Journal of Chemical Physics 115 (2001) 1213.
[66] G. Herzberg, Molecular Spectra and Molecular Structure. I. Spectra of Diatomic Molecules, Van Nostrand, New York, 1950.
[67] M.J. Frisch, G.W. Trucks, H.B. Schlegel, G.E. Scuseria, M.A. Robb, J.R. Cheeseman, G. Scalmani, V. Barone, B. Mennucci, G.A. Petersson, H. Nakatsuji, M. Caricato, X. Li, H.P. Hratchian, A.F. Izmaylov, J. Bloino, G. Zheng, J.L. Sonnenberg, M. Hada, M. Ehara, K. Toyota, R. Fukuda, J. Hasegawa, M. Ishida, T. Nakajima, Y. Honda, O. Kitao, H. Nakai, T. Vreven, J.A. Montgomery Jr., J.E. Peralta, F. Ogliaro, M. Bearpark, J.J. Heyd, E. Brothers, K.N. Kudin, V.N. Staroverov, R. Kobayashi, J. Normand, K. Raghavachari, A. Rendell, J.C. Burant, J.M. Millam, S.S. Iyengar, J. Tomasi, M. Cossi, N. Rega, J.M. Millam, M. Klene, J.E. Knox, J.B. Cross, V. Bakken, C. Adamo, J. Jaramillo, R. Gomperts, R.E. Stratmann, O. Yazyev, A.J. Austin, R. Cammi, C. Pomelli, J.W. Ochterski, R.L. Martin, K. Morokuma, V.G. Zakrzewski, G.A. Voth, P. Salvador, J.J. Dannenberg, S. Dapprich, A.D. Daniels, O. Farkas, J.B. Foresman, J.V. Ortiz, J. Cioslowski, D.J. Fox, Gaussian 09 Revision A. 02, Gaussian, Inc., Wallingford, CT, 2009.
[68] A.D. Becke, Journal of Chemical Physics 98 (1993) 5648.
[69] C. Lee, W. Yang, R.G. Parr, Physical Review B 37 (1988) 785.
[70] A.D. Becke, Journal of Chemical Physics 98 (1993) 1372.
[71] A.D. Becke, Physical Review A 38 (1988) 3098.
[72] J.P. Perdew, Physical Review B 33 (1986) 8822.
[73] K. Raghavachari, G.W. Trucks, J.A. Pople, M. Head-Gordon, Chemical Physics Letters 157 (1989) 479.
[74] R.J. Bartlett, J.D. Watts, S.A. Kucharski, J. Noga, Chemical Physics Letters 165 (1990) 513.
[75] G.E. Scuseria, T.J. Lee, Journal of Chemical Physics 93 (1990) 5851.
[76] T.D. Crawford, J.F. Stanton, International Journal of Quantum Chemistry 70 (1998) 601.
[77] F. Furche, J.P. Perdew, Journal of Chemical Physics 124 (2006) 044103.
[78] T.G. Rowland, B. Sztaray, P.B. Armentrout, Journal of Physical Chemistry A 117 (2013) 1299.
[79] M.J. Frisch, J.A. Pople, J.S. Binkley, Journal of Chemical Physics 80 (1984) 3265.
[80] M.W. Chase, C.A. Davies, J.R. Downey, D.J. Frurip, R.A. McDonald, A.N. Syverud, Journal of Physical Chemistry Reference Data 14 (Suppl. 1) (1985) 1.
[81] F. Weigand, R. Aldrichs, Physical Chemistry Chemical Physics 7 (2005) 3297.
[82] M. Dolg, H. Stoll, H. Preuss, R.M. Pitzer, Journal of Physical Chemistry 87 (1993) 5852.
[83] D. Andrae, U. Haeussermann, M. Dolg, H. Stoll, H. Preuss, Theoretical Chemistry Accounts 77 (1990) 123.
[84] P.J. Hay, W.R. Wadt, Journal of Chemical Physics 82 (1985) 299.
[85] D.J. Feller, Journal of Computational Chemistry 17 (1996) 1571.
[86] K.L. Schuchardt, B.T. Didier, T. Elsethagen, L. Sun, V. Gurumoorthi, J. Chase, J. Li, T.L. Windus, Journal of Chemical Information and Modeling 47 (2007) 1045.
[87] G. Ohanessian, M.J. Brusich, W.A. Goddard III, Journal of the American Chemical Society 112 (1990) 7179.
[88] J.B. Foresman, A.E. Frisch, Exploring Chemistry with Electronic Structure Methods, Guassian, Inc., Pittsburgh, PA, 1996.
[89] G. Gioumousis, D.P. Stevenson, Journal of Physical Chemistry 29 (1958) 294.
[90] E.W. Rothe, R.B. Bernstein, Journal of Chemical Physics 31 (1959) 1619.
[91] A.A. Radzig, B.M. Smirnov, Reference Data on Atoms, Molecules, and Ions, Springer-Verlag, Berlin, 1985.
[92] C. Rue, P.B. Armentrout, I. Kretzschmar, D. Schröder, J.N. Harvey, H. Schwarz, Journal of Chemical Physics 110 (1999) 7858.
[93] G.F. Stowe, R.H. Schultz, C.A. Wight, P.B. Armentrout, International Journal of Mass Spectrometry and Ion Processes 100 (1990) 177.
[94] R.S. Ram, J. Liévin, P.F. Bernath, Journal of Chemical Physics 111 (1999) 3449.
[95] M.A. Garcia, M.D. Morse, Journal of Chemical Physics 135 (2011) 114304.
[96] H. Lefebvre-Brion, R.W. Field, The Spectra and Dynamics of Diatomic Molecules, Elsevier, Amsterdam, 2004.
[97] M.C. Holthausen, M. Mohr, W. Koch, Chemical Physics Letters 240 (1995) 245.
[98] I. Kretzschmar, A. Fiedler, J.N. Harvey, D. Schröder, H. Schwarz, Journal of Physical Chemistry A 101 (1997) 6252.
[99] Journal of Chemical Physics 23 (1955) 1997.